

# A Combined Ordered Macro-Mesoporous Architecture Design and Surface Engineering Strategy for High-Performance Sulfur Immobilizer in Lithium–Sulfur Batteries

Guihua Liu, Dan Luo, Rui Gao, Yongfeng Hu, Aiping Yu, and Zhongwei Chen\*

The practical application of lithium–sulfur (Li–S) batteries is hindered by the “shuttle” of lithium polysulfides (LiPS) and sluggish Li–S kinetics issues. Herein, a synergistic strategy combining mesoporous architecture design and defect engineering is proposed to synthesize multifunctional defective 3D ordered mesoporous cobalt sulfide (3DOM N-Co<sub>9</sub>S<sub>8-x</sub>) to address the shuttling and sluggish reaction kinetics of polysulfide in Li–S batteries. The unique 3DOM design provides abundant voids for sulfur storage and enlarged active interfaces that reduce electron/ion diffusion pathways. Meanwhile, X-ray absorption spectroscopy shows that the surface defect engineering tunes the CoS<sub>4</sub> tetrahedra to CoS<sub>6</sub> octahedra on Co<sub>9</sub>S<sub>8</sub>, endowing abundance of S vacancies on the Co<sub>9</sub>S<sub>8</sub> octahedral sites. The ever-increasing S vacancies over the course of electrochemical process further promotes the chemical trapping of LiPS and its conversion kinetics, rendering fast and durable Li–S chemistry. Benefiting from these features, the as-developed 3DOM N-Co<sub>9</sub>S<sub>8-x</sub>/S cathode delivers high areal capacity, superb rate capability, and excellent cyclic stability with ultralow capacity fading rate under raised sulfur loading and low electrolyte content. This design strategy promotes the development of practically viable Li–S batteries and sheds lights on the material engineering in related energy storage application.

hindered by many obstacles, such as the insulating nature of sulfur, notorious shuttle effect of lithium polysulfides (LiPS), sluggish redox reaction and large volume variation during charge–discharge process.<sup>[2]</sup> The state-of-art strategy to deal with these problems is to develop a conductive multifunctional sulfur host or barrier material that can physically/chemically confine LiPS, leading to enhanced inhibition of polysulfide shuttling effect and improved catalytic performance toward rapid LiPS conversion.<sup>[3]</sup>

Porous carbonaceous materials and their composites with transitional metal oxides (TMOs) are the most widely studied sulfur immobilizers in Li–S batteries.<sup>[4]</sup> Carbon materials can establish an electronic conductive network, whereas the porous structure can offer large surface area to homogenize sulfur distribution and enhanced physical sulfur confinement.<sup>[5]</sup> Due to the strong sulfur immobilization on polar oxides surface, the introduction of TMOs can further

## 1. Introduction

Owing to its high energy density, environmental benignity and low cost, lithium–sulfur (Li–S) batteries have been considered as a promising next-generation energy storage system.<sup>[1]</sup> However, the practical application of Li–S batteries is still

mitigate the shuttle effect of LiPS.<sup>[6]</sup> However, most of these multifunctional sulfur host materials still cannot meet the requirements for the practical application of Li–S battery, especially under high sulfur loading and lean electrolyte/sulfur (E/S) ratio condition.<sup>[7]</sup> The inadequate electrochemical performance under such operating condition might originate from the structural design of sulfur host materials. For example, most of the reported sulfur host composites are carbon supported materials. Under raised sulfur loading, the porous structure of carbon substrates is usually unstable and tends to crack during the Li–S charge/discharge process.<sup>[8]</sup> In addition, the catalytic performance of supported TMOs is still unsatisfactory, affording an insufficient Li–S reaction kinetics.<sup>[9]</sup> Recently, highly electrocatalytic active transitional metal sulfides (TMSs) were developed as multifunctional sulfur immobilizer to promote the electrochemical redox process, which is very effective to improve the utilization of sulfur and enhance the LiPS catalytic conversion.<sup>[10]</sup> Furthermore, TMSs are favorable in achieving fast ion/electron transfer process for sulfur cathode owing to its high conduction properties.<sup>[11]</sup> Therefore, a selection of sulfur host material with decent ion/electron conduction, proper structural design with enhanced structural stability and abundant LiPS trapping/catalytic active

Dr. G. Liu  
Tianjin Key Laboratory of Chemical Process Safety  
School of Chemical Engineering and Technology  
Hebei University of Technology  
Tianjin 300130, China

Dr. G. Liu, D. Luo, Dr. R. Gao, Prof. A. Yu, Prof. Z. Chen  
Department of Chemical Engineering  
University of Waterloo  
Waterloo, Ontario N2L 3G1, Canada  
E-mail: zhwchen@uwaterloo.ca

Dr. Y. Hu  
Canadian Light Source  
University of Saskatchewan  
Saskatoon, Saskatchewan S7N 0X4, Canada

 The ORCID identification number(s) for the author(s) of this article can be found under <https://doi.org/10.1002/smll.202001089>.

DOI: 10.1002/smll.202001089

sites is essential in the development of high-performance Li–S batteries.

Herein, we developed a synergistic strategy combining the design of 3D ordered mesoporous (3DOM) structure with facile surface engineering technique to develop efficient sulfur immobilizer toward superior Li–S electrochemistry. This strategy is demonstrated by the successful fabrication of a 3DOM S-deficient N-Co<sub>9</sub>S<sub>8-x</sub> composite via a hard template method. The Co<sub>9</sub>S<sub>8</sub>, as a typical transition metal chalcogenides (TMCs), is selected owing to its higher conductivity and LiPS catalytic activity.<sup>[12]</sup> The 3DOM design offers abundant surface area and large porosity to host active sulfur species, reserve electrolyte and accommodate volume expansion during sulfur lithiation. Meanwhile, the surface chemical property that contributed to the enhanced LiPS adsorption and rapid conversion kinetics was thoroughly investigated by the X-ray absorption spectroscopy (XAS) technique and theoretical calculations. It was found that the defect engineering, through a facile ammonia treatment, introduces N substitution on the surface of Co<sub>9</sub>S<sub>8</sub>, tuning part of CoS<sub>4</sub> tetrahedron into CoS<sub>6</sub> octahedra, leading to the formation of numerous S vacancies on the octahedral Co sites. These S vacancies further evolves and gradually increases over the course of electrochemical process, which offers ever-increasing active sites to strengthen LiPS adsorptive and catalytic properties. Benefited from these advantages, the 3DOM

N-Co<sub>9</sub>S<sub>8-x</sub>/S cathode delivers superior cyclability with a low capacity fading rate of 0.04% per cycle over 500 cycles at 1 C, an admirable rate capability up to 5 C and high areal capacity over 5.9 mAh cm<sup>-2</sup> under raised sulfur loading and decreased E/S ratio, offering great promises to be used for practically viable Li–S batteries.

## 2. Results and Discussion

Figure 1a shows the synthetic process of 3DOM N-Co<sub>9</sub>S<sub>8-x</sub>, which illustrated the synergy of architecture design and defect engineering to construct a multifunctional substrate for enhanced Li–S electrochemistry. The 3DOM structure was constructed by using polystyrene (PS) spheres as template obtained by the self-assembly method.<sup>[13]</sup> The SEM morphology of PS spheres is shown in Figure S1 in the Supporting Information, revealing its size uniformity. During the pyrolysis process under Ar atmosphere, the soaked metal sulfate precursor in the void of PS spheres was converted into Co<sub>9</sub>S<sub>8</sub>, whereas the PS template will decompose, forming large interconnected pore structure. The formation of Co<sub>9</sub>S<sub>8</sub> might result from the chemical reaction listed below

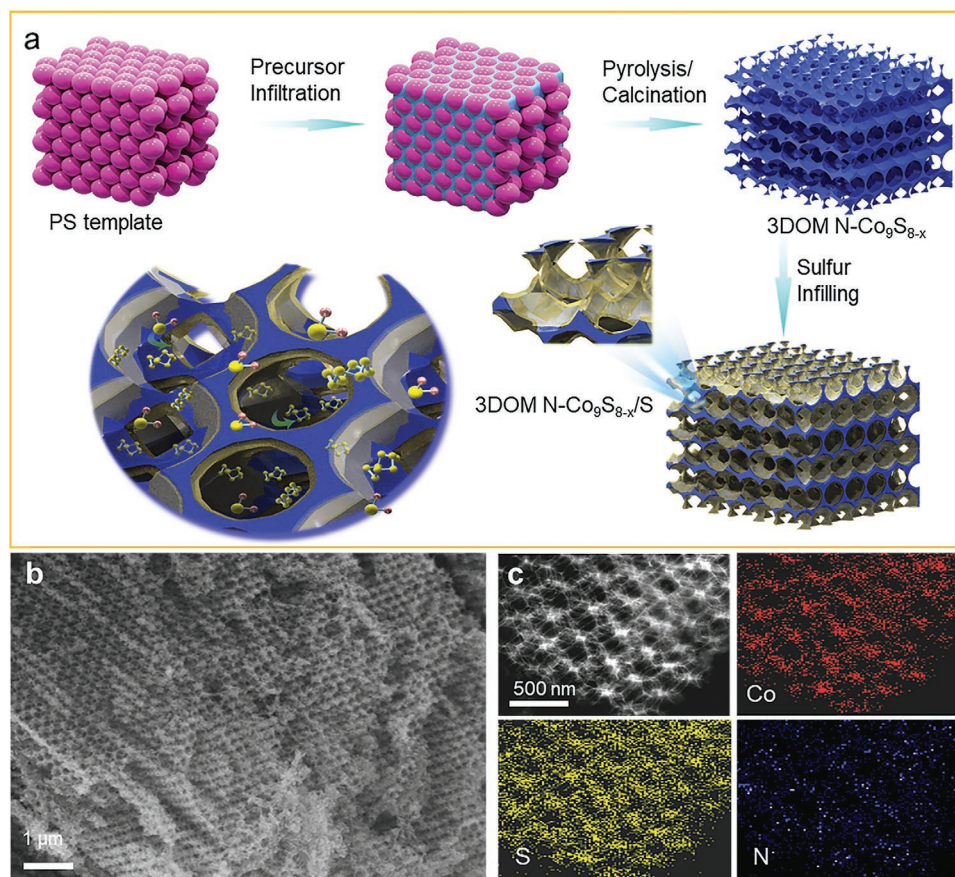


**Figure 1.** a) Scheme illustration for the synthetic strategy of 3DOM N-Co<sub>9</sub>S<sub>8-x</sub> and its sulfur composites; b) SEM image of 3DOM N-Co<sub>9</sub>S<sub>8-x</sub>; c) The STEM and corresponding EDX element mappings of 3DOM N-Co<sub>9</sub>S<sub>8-x</sub>.

Subsequently, the  $\text{NH}_3$  etching introduces vast defects including N substitution and S vacancies into 3DOM  $\text{Co}_9\text{S}_8$  (noted as 3DOM N- $\text{Co}_9\text{S}_{8-x}$ ). A mild surface oxidation of 3DOM N- $\text{Co}_9\text{S}_{8-x}$  is also observed in XPS spectrum, which might resulted from residual  $\text{CoSO}_4$  or its exposure in air. The morphology of 3DOM N- $\text{Co}_9\text{S}_{8-x}$  is revealed in Figure 1b. Clearly, the material still keeps its intact structure and porosity without damage, indicating its good structure stability and good controllability of defect engineering strategy. The scanning transmission electron microscopy (STEM) image and corresponding EDX element mapping in Figure 1c implies a homogeneous element distribution of Co, S, and N. TGA analysis indicates a high  $\text{Co}_9\text{S}_8$  content of 90.1% in 3DOM N- $\text{Co}_9\text{S}_{8-x}$  (Figure S2, Supporting Information).

To evaluate the advantages of structure design and defect engineering,  $\text{Co}_9\text{S}_8$  nanoparticle ( $\text{Co}_9\text{S}_8$  NPs) and vacancy-free 3DOM  $\text{Co}_9\text{S}_8$ , were also synthesized. The detailed synthetic

process can be found in Supporting Information. The XRD pattern in Figure 2a shows that all these materials have typical diffraction pattern of  $\text{Co}_9\text{S}_8$ . As compared with 3DOM  $\text{Co}_9\text{S}_8$  and  $\text{Co}_9\text{S}_8$  NPs, the positive shift of XRD peaks in 3DOM N- $\text{Co}_9\text{S}_{8-x}$  suggests the shrinkage of  $\text{Co}_9\text{S}_8$  crystal owing to its structure distortion induced by the defect engineering. Figure 2b exhibits the surface area and pore size distribution of 3DOM N- $\text{Co}_9\text{S}_{8-x}$ , which reveals its high BET surface area of  $149.4 \text{ m}^2 \text{ g}^{-1}$  and hierarchical porosity with a high pore volume of  $0.43 \text{ cm}^3 \text{ g}^{-1}$ . SEM images of 3DOM  $\text{Co}_9\text{S}_8$  and  $\text{Co}_9\text{S}_{8-x}$  all exhibit good size uniformity and plentiful porosity (Figure 2c,d). The HRTEM and corresponding fast Fourier transformation (FFT) images of 3DOM  $\text{Co}_9\text{S}_{8-x}$  are shown in Figure 2e,f, which confirmed the crystalline feature of  $\text{Co}_9\text{S}_8$ . This hierarchical porous 3DOM N- $\text{Co}_9\text{S}_{8-x}$  skeleton offers abundant active surface area, large hollow interior and hierarchical porosity, which homogenizes sulfur distribution, alleviates volume expansion during sulfur

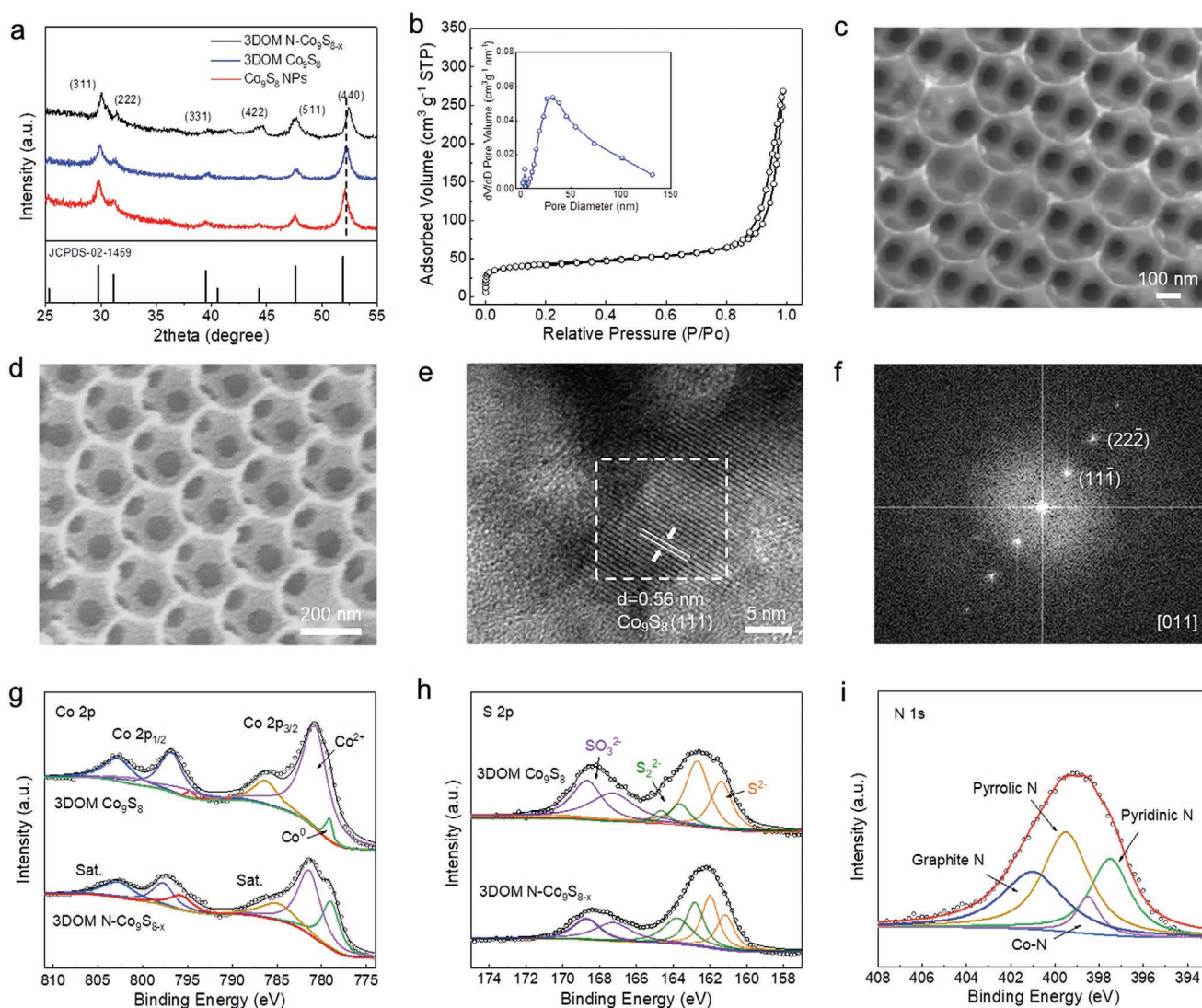


**Figure 2.** a) XRD pattern of  $\text{Co}_9\text{S}_8$  NPs, 3DOM  $\text{Co}_9\text{S}_8$ , and 3DOM N- $\text{Co}_9\text{S}_{8-x}$ ; b)  $\text{N}_2$  adsorption–desorption isotherms curves and the corresponding pore size distribution of 3DOM N- $\text{Co}_9\text{S}_{8-x}$ ; c) The SEM image of 3DOM  $\text{Co}_9\text{S}_8$  and d) 3DOM N- $\text{Co}_9\text{S}_{8-x}$ ; e) HRTEM image and corresponding. f) FFT image of 3DOM N- $\text{Co}_9\text{S}_{8-x}$ ; g) Co 2p, and h) S 2p high-resolution XPS spectra of 3DOM  $\text{Co}_9\text{S}_8$  and 3DOM N- $\text{Co}_9\text{S}_{8-x}$ . i) N 1s XPS spectrum of 3DOM N- $\text{Co}_9\text{S}_{8-x}$ .

lithiation and shorts electrolyte diffusion pathway as well as facilitates ion/electron transportation within the electrode.

To investigate the benefit of defect engineering, the surface chemistry of  $\text{Co}_9\text{S}_8$  materials are analyzed by XPS. In Figure 2g and Figure S3a in the Supporting Information, in addition to the  $\text{Co}^{2+}$  state, the Co 2p spectrum of 3DOM N- $\text{Co}_9\text{S}_{8-x}$  shows a more distinctive metallic  $\text{Co}^0$  state ( $2p_{3/2}$  peak at 778.2 eV) than those of 3DOM  $\text{Co}_9\text{S}_8$  and  $\text{Co}_9\text{S}_8$  NPs, suggesting its reduced surface state of Co by S vacancy.<sup>[14]</sup> The S 2p spectra in Figure 2h and Figure S3b (Supporting Information) show three sets of peaks located between 160 and 168 eV, which can be ascribed to  $\text{S}^{2-}$ ,  $\text{S}_2^{2-}$ , and  $\text{SO}_x^{2-}$ .<sup>[15]</sup> Clearly, 3DOM N- $\text{Co}_9\text{S}_{8-x}$  demonstrates the lowest  $\text{SO}_x^{2-}$  species intensity and an intensified  $\text{S}_2^{2-}/\text{S}^{2-}$  ratio among the three samples, further confirming its reduced nature.<sup>[16]</sup> The N 1s spectrum of 3DOM N- $\text{Co}_9\text{S}_{8-x}$  shows the existence of N doped carbon, e.g. pyrrolic-N (399.5 eV), pyridinic-N (397.5 eV), and N-insertion in the

bulk  $\text{Co}_9\text{S}_8$  crystal (398.5 eV) as well,<sup>[17]</sup> see Figure 2i. Moreover, the atomic composition of XPS analysis reveals a similar S/Co atomic ratio between  $\text{Co}_9\text{S}_8$  NPs and 3DOM  $\text{Co}_9\text{S}_8$ , which closes to the theoretical S/Co value of  $\text{Co}_9\text{S}_8$  (0.89). However, this ratio in 3DOM N- $\text{Co}_9\text{S}_{8-x}$  is decreased to 0.79, indicating the formation of S-deficient  $\text{Co}_9\text{S}_8$ .<sup>[18]</sup>

The defect and crystal structure distortion of 3DOM N- $\text{Co}_9\text{S}_{8-x}$  were further investigated by X-ray absorption near-edge structure (XANES), extended X-ray absorption fine structure (EXAFS), electron energy-loss near-edge spectroscopy (ELNES) and electron paramagnetic resonance spectroscopy (EPR). After  $\text{NH}_3$  treatment, part of sulfur atom was removed, inducing the formation of S-deficient  $\text{Co}_9\text{S}_8$  structure. The cubic structure  $\text{Co}_9\text{S}_8$  is constituted by  $\text{CoS}_6$  octahedra and  $\text{CoS}_4$  tetrahedra with a ratio of 1:8 (Figure 3a) while  $\text{CoS}_2$  only contains  $\text{CoS}_6$  octahedra in its crystal structure (Figure S4, Supporting Information). To further analyze the content variation, the XAS

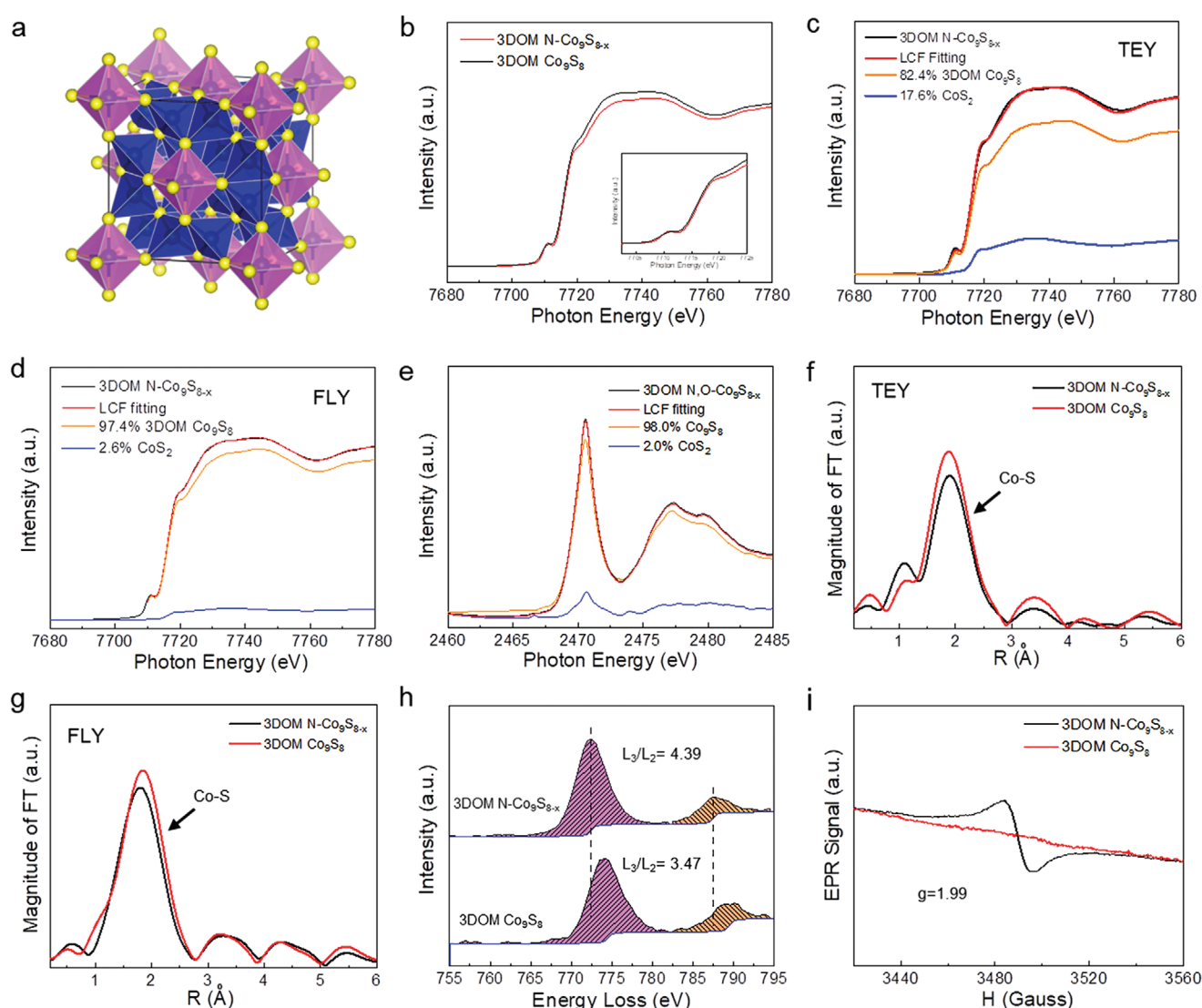


**Figure 3.** a) Crystal structure of  $\text{Co}_9\text{S}_8$ , b) The Co K-edge XANES spectra of 3DOM  $\text{Co}_9\text{S}_8$  and 3DOM N- $\text{Co}_9\text{S}_{8-x}$ ; c, d) Co K-edge and e) S K-edge XANES spectra of 3DOM N- $\text{Co}_9\text{S}_{8-x}$  and the corresponding linear combination fitting spectra; FT  $k^3$ -weighted Co K-edge EXAFS spectra of f) TEY mode and g) FLY mode; h) Co  $L_{2,3}$ -edge ELNES spectra of 3DOM  $\text{Co}_9\text{S}_8$  and 3DOM N- $\text{Co}_9\text{S}_{8-x}$ ; i) EPR signal of 3DOM  $\text{Co}_9\text{S}_8$  and 3DOM N- $\text{Co}_9\text{S}_{8-x}$ .

spectra of 3DOM N-Co<sub>9</sub>S<sub>8-x</sub>, 3DOM N-Co<sub>9</sub>S<sub>8</sub> were collected and compared. The CoS<sub>2</sub> spectrum was collected as reference, which represents the structure information of CoS<sub>6</sub> octahedra. Figure 3b shows the XANES spectra of 3DOM Co<sub>9</sub>S<sub>8</sub> and 3DOM N-Co<sub>9</sub>S<sub>8-x</sub> in fluorescence yield (FLY) mode, which reveals the similar peak shape and adsorption edge ( $E_0$ ), indicating the same valence state of Co in the bulk type of these samples. To identify the CoS<sub>6</sub> octahedra augmented affected by defect engineering and the defective state on the surface and bulk of material, the principal component analysis and linear combination fitting (PCA-LCF) of Co *K*-edge XANES for 3DOM Co<sub>9</sub>S<sub>8</sub> and 3DOM N-Co<sub>9</sub>S<sub>8-x</sub> was applied for both the surface sensitive total electron yield (TEY) spectra and FLY spectra (Figure 3c,d). The perfectly matched XANES results and fitting curves for both TEY and FLY indicate a higher CoS<sub>6</sub> content of 17.6% in 3DOM N-Co<sub>9</sub>S<sub>8-x</sub> in the TEY than FLY, suggesting that more CoS<sub>6</sub> octahedra is formed on the surface of 3DOM N-Co<sub>9</sub>S<sub>8-x</sub>. The 2% CoS<sub>6</sub> content increase is further revealed by LCF fitting results of S *K*-edge XANES spectrum under FLY mode (Figure 3e), which is similar with LCF fitting results of Co *K*-edge XANES spectrum. Figure 3f,g demonstrates Co *K*-edge EXAFS Fourier transform of 3DOM Co<sub>9</sub>S<sub>8</sub> and 3DOM N-Co<sub>9</sub>S<sub>8-x</sub> in both TEY and FLY modes, in which the first shell located at 1.87 Å can be assigned to Co–S coordination. The EXAFS results display reduced peak intensity, indicating the decrease of coordination number owing to the formation of S vacancies in 3DOM N-Co<sub>9</sub>S<sub>8-x</sub>. These results indicate that the defect engineering strategy tunes some of the CoS<sub>4</sub> tetrahedron into CoS<sub>6</sub> octahedra and creates S vacancies on the octahedra sites for 3DOM N-Co<sub>9</sub>S<sub>8-x</sub>. To verify this point, ELNES spectra were also provided (Figure 3h) to identify its structural distortion on the surface. ELNES can reflect the L-edge feature of Co, which is sensitive to the changes of valence state and high spatial resolution. The Co L<sub>2,3</sub>-edge ELNES spectrum of 3DOM Co<sub>9</sub>S<sub>8</sub> reveals a L<sub>3</sub>/L<sub>2</sub> intensity ratio of 3.47, corresponding to an average Co valence of Co<sup>2.5+</sup>.<sup>[19]</sup> Comparing with 3DOM Co<sub>9</sub>S<sub>8</sub>, the Co L<sub>3</sub> peak in 3DOM N-Co<sub>9</sub>S<sub>8-x</sub> undergoes negative shifts and the L<sub>3</sub>/L<sub>2</sub> intensity ratio increased to 4.39, suggesting that the Co valence was reduced to Co<sup>2.1+</sup> on the surface, which is consistent with XPS analysis.<sup>[20]</sup> The EPR pattern in Figure 3i shows a signal with a *g* value of 1.99, suggesting the existence of S vacancies inside 3DOM N-Co<sub>9</sub>S<sub>8-x</sub>.<sup>[21]</sup> All these results affirmed that the introduction of N substitution inside Co<sub>9</sub>S<sub>8</sub> partially alters CoS<sub>4</sub> tetrahedron into CoS<sub>6</sub> octahedra, leading to the formation of S vacancies on octahedral sites. The defective surface offers multiple active sites to amplify LiPS adsorption and conversion process toward superior kinetics, showing great promises to be utilized in Li–S batteries for performance enhancement.

To verify the enhanced LiPS adsorbability of N-Co<sub>9</sub>S<sub>8-x</sub> on the defective sites, the LiPS binding energies on Co<sub>9</sub>S<sub>8</sub> and N-Co<sub>9</sub>S<sub>8-x</sub> (311) surface were calculated by density functional theory (DFT). Detailed information on the computational method and model construction can be found in the Supporting Information. The results show that N-Co<sub>9</sub>S<sub>8-x</sub> exhibits a higher binding energy than that on ideal Co<sub>9</sub>S<sub>8</sub> for all the Li<sub>2</sub>S<sub>2</sub>, Li<sub>2</sub>S<sub>6</sub>, and Li<sub>2</sub>S<sub>4</sub> species (Figure 4a). The optimized adsorption configuration reveals that additional Co–S bonding was formed between LiPS species and the defective Co<sub>9</sub>S<sub>8-x</sub>

surface in N-Co<sub>9</sub>S<sub>8-x</sub>, which might contribute to its enhanced binding energy. In addition, the strengthened chemical interaction between LiPS and N-Co<sub>9</sub>S<sub>8-x</sub> is further revealed by XPS analysis (Figure 4b,c). It can be clearly observed that, after Li<sub>2</sub>S<sub>6</sub> adsorption, both Co 2p<sub>1/2</sub> and Co 2p<sub>3/2</sub> peaks of 3DOM N-Co<sub>9</sub>S<sub>8-x</sub>-Li<sub>2</sub>S<sub>6</sub> shift to higher binding energy region. Meanwhile, the larger shift of S<sub>T</sub><sup>-1</sup> and S<sub>B</sub><sup>0</sup> peaks in the 3DOM N-Co<sub>9</sub>S<sub>8-x</sub>-Li<sub>2</sub>S<sub>6</sub> indicates reduced electron density of S in LiPS.<sup>[22]</sup> The visualized adsorption experiments of Li<sub>2</sub>S<sub>6</sub> solution by different adsorbents were further conducted, as shown in Figure S5 in the Supporting Information. Comparing with Co<sub>9</sub>S<sub>8</sub> NPs, the Li<sub>2</sub>S<sub>6</sub> solution became much clearer after adsorption test by 3DOM N-Co<sub>9</sub>S<sub>8</sub>, confirming its enhanced LiPS adsorption capability. The 3DOM N-Co<sub>9</sub>S<sub>8-x</sub>-Li<sub>2</sub>S<sub>6</sub> solution shows the most transparent color, indicating its strongest LiPS adsorption capability. The Li<sub>2</sub>S<sub>6</sub> UV–vis spectra in Figure S6 in the Supporting Information showed significant decrease in peak intensity after adsorption by 3DOM N-Co<sub>9</sub>S<sub>8-x</sub>, indicating its strong LiPS chemical confinement, as consistent with visualized adsorption results. The structural distortion of 3DOM N-Co<sub>9</sub>S<sub>8-x</sub> and its interaction with LiPS during discharge–charge process is further verified by Co *K*-edge ex-situ XANES and EXAFS measurements. The Co<sub>9</sub>S<sub>8</sub> XANES spectrum simulation based on Fdmnes code is shown in Figure S7 in the Supporting Information.<sup>[23]</sup> Notably, as the CoS<sub>4</sub> tetrahedra content increases, the energy jump of peak A and B shifts to lower photon energy region while no obvious jump occurred on peak C. However, due to the self-adsorption of material, the peak B of Co<sub>9</sub>S<sub>8</sub> delivers a low intensity in real XANES spectra. The analysis of these features can be used to determine the CoS<sub>6</sub> content variation of 3DOM N-Co<sub>9</sub>S<sub>8-x</sub> in the course of electrochemical process. Figure 4d shows the evolution of Co *K*-edge XANES spectra of 3DOM N-Co<sub>9</sub>S<sub>8-x</sub>/S during the initial discharge and charge process. In the discharge process, the positive shifts of peak A and B coupling with the increased intensity of peak C after discharged to 2.15 and 1.8 V indicates that more CoS<sub>6</sub> octahedra was formed in 3DOM N-Co<sub>9</sub>S<sub>8-x</sub>. Meanwhile, the amplitude of Co–S coordination at 1.7 Å is much lower for the discharged samples, which suggests a low coordination number of Co–S for discharged samples (Figure 4e). Since the Co–S bond length of CoS<sub>6</sub> octahedra is larger than that of CoS<sub>4</sub> tetrahedra, the slightly increased radial distance can be explained by the formation of more CoS<sub>6</sub> octahedra in 3DOM N-Co<sub>9</sub>S<sub>8-x</sub>, which is consistent with its structural transformation.<sup>[24]</sup> In addition, the decreased coordination number of Co–S at discharge state indicates its greater structure distortion attributed to the increased defects. In the charge process, the peak A and B shifts back to low energy region while the intensity of peak C decreased after charged to 2.6 V, indicating its increased CoS<sub>4</sub> tetrahedra content. In addition, the EXAFS spectrum also witnesses a backward shift of radial distance after charged to 2.6 V, corresponding to the augmentation of CoS<sub>4</sub> tetrahedra in the 3DOM N-Co<sub>9</sub>S<sub>8-x</sub>. However, a decreased Co–S coordination number can still be observed after fully charged, which indicates the ever-increasing S vacancies. Therefore, the defective structure of 3DOM N-Co<sub>9</sub>S<sub>8-x</sub> is highly dynamic and evolves over the course of electrochemical process, which induces more S vacancies formation. The amplified S vacancies, in return, offers abundant active sites to accelerate the

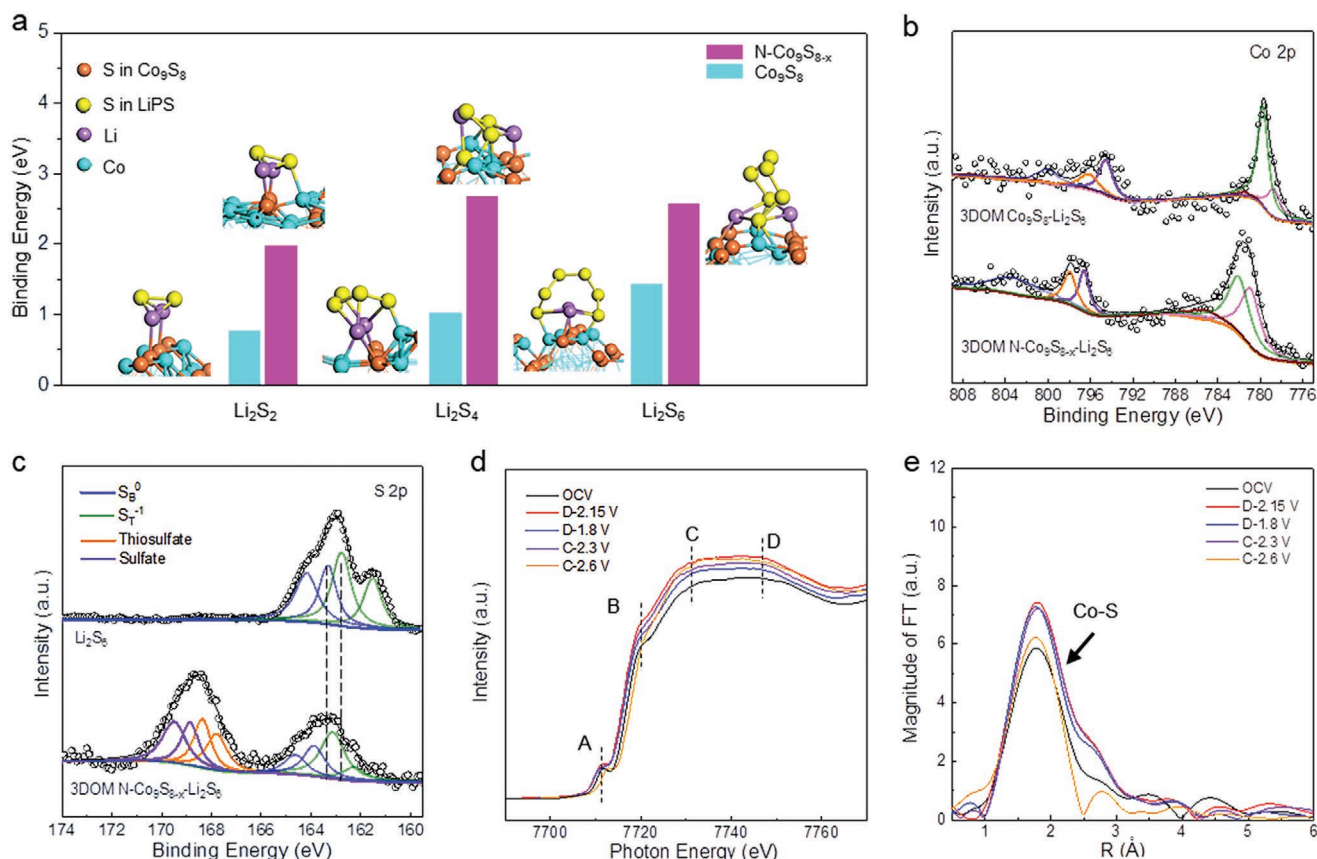


**Figure 4.** a) DFT optimized binding energies and geometries of  $\text{Li}_2\text{S}_2$ ,  $\text{Li}_2\text{S}_4$ , and  $\text{Li}_2\text{S}_6$  adsorption on 3DOM  $\text{Co}_9\text{S}_8$  and 3DOM  $\text{N-Co}_9\text{S}_{8-x}$ ; b) Co 2p and c) S 2p XPS spectra of 3DOM  $\text{Co}_9\text{S}_8$  and 3DOM  $\text{N-Co}_9\text{S}_{8-x}$  after  $\text{Li}_2\text{S}_6$  adsorption; d) Evolution of Co K-edge XANES spectra and e) FT  $k^2$ -weighted Co K-edge EXAFS spectra of 3DOM  $\text{N-Co}_9\text{S}_{8-x}/\text{S}$  cathode in the first discharge–charge process (OCV: open circuit voltage, D - 2.15 V: discharged to 2.15 V, D - 1.8 V: discharged to 1.8 V, C - 2.3 V: charged to 2.3 V, C - 2.6 V: charged to 2.6 V).

LiPS catalytic conversion, rendering favoured redox reaction. The DFT, UV–vis spectra, XPS, and XAS results strongly support that defective sites remarkably improve LiPS adsorption on 3DOM  $\text{N-Co}_9\text{S}_{8-x}$ , fulfilling the requirement to be utilized as multifunctional sulfur immobilizer.

Symmetrical cells were assembled to evaluate the promoted LiPS conversion kinetics on the 3DOM  $\text{N-Co}_9\text{S}_{8-x}$  interface. Figure 5a–c demonstrates the CV curves with different scan rates of 3DOM  $\text{N-Co}_9\text{S}_{8-x}$ , 3DOM  $\text{Co}_9\text{S}_8$ , and  $\text{Co}_9\text{S}_8$  NPs, respectively. The distinctive redox peaks represent the multi-step LiPS conversion reactions. The redox current density is linear correlation with the square root of the scan rate, suggesting a strong diffusion-controlled feature for LiPS conversion. Clearly, 3DOM  $\text{N-Co}_9\text{S}_{8-x}$  electrode demonstrates the best  $\text{Li}^+$  diffusion capability with the highest diffusion coefficient ( $D_{\text{Li}^+}$ ,  $1.67 \times 10^{-10} \text{ cm}^2 \text{ s}^{-1}$ ), comparing with 3DOM  $\text{Co}_9\text{S}_8$  ( $6.58 \times 10^{-11} \text{ cm}^2 \text{ s}^{-1}$ ) and  $\text{Co}_9\text{S}_8$  NPs ( $8.18 \times 10^{-12} \text{ cm}^2 \text{ s}^{-1}$ ), indicating its best ion diffusion process (Figure 5d). The catalytic effect of these materials were further evaluated in symmetrical cells, containing  $\text{Li}_2\text{S}_8$  in electrolyte (Figure S8, Supporting Information). All these CV curves demonstrate two reduction peaks at  $-0.3$  and  $-0.55$  V, corresponding to the reduction of  $\text{Li}_2\text{S}_8$  to  $\text{Li}_2\text{S}_4$  and its further reduction to  $\text{Li}_2\text{S}$ . The 3DOM  $\text{N-Co}_9\text{S}_{8-x}$  exhibits the highest redox current

response, indicating its best LiPS conversion kinetics for favoured redox reactions. In Figure S9 in the Supporting Information, the 3DOM  $\text{N-Co}_9\text{S}_{8-x}$  exhibits the smallest resistance and highest redox current density, confirming the accelerated redox reactions. To further demonstrate the enhanced catalytic behavior and fast LiPS conversion process, potentiostatic discharge profiles of  $\text{Li}_2\text{S}_8/\text{tetraglyme}$  solution at 2.05 V were collected, as shown in Figure 5e,f. On the basis of calculating the integral of the current, the capacities of  $\text{Li}_2\text{S}$  precipitation on 3DOM  $\text{N-Co}_9\text{S}_{8-x}$  is evidently higher than that of 3DOM  $\text{Co}_9\text{S}_8$ , manifesting the superior activity and conversion behavior. The catalytic behaviour of 3DOM  $\text{N-Co}_9\text{S}_{8-x}$  was further elucidated by linear scanning voltammetry (LSV) techniques within  $\text{Li}_2\text{S}_6$  catholyte solution. The accelerated catalytic performance of 3DOM  $\text{N-Co}_9\text{S}_{8-x}$  is verified by its higher exchange current density of  $0.14 \text{ mA cm}^{-2}$  than that of 3DOM  $\text{Co}_9\text{S}_8$  ( $0.046 \text{ mA cm}^{-2}$ ) in Tafel plots (Figure 5g).<sup>[25]</sup> Also, the LiPS conversion kinetics on  $\text{N-Co}_9\text{S}_{8-x}$  was studied by calculating the energetics of  $\text{Li}_2\text{S}_2$  decomposition pathway (Figure 5h). The results show that  $\text{Li}_2\text{S}_2$  need to overcome a much lower barrier of 0.68 eV on  $\text{N-Co}_9\text{S}_{8-x}$  than that on ideal  $\text{Co}_9\text{S}_8$  (1.02 eV). Overall, the defective  $\text{N-Co}_9\text{S}_{8-x}$  shows enhanced catalytic performance, achieving high kinetics toward Li–S electrochemistry.<sup>[26]</sup>

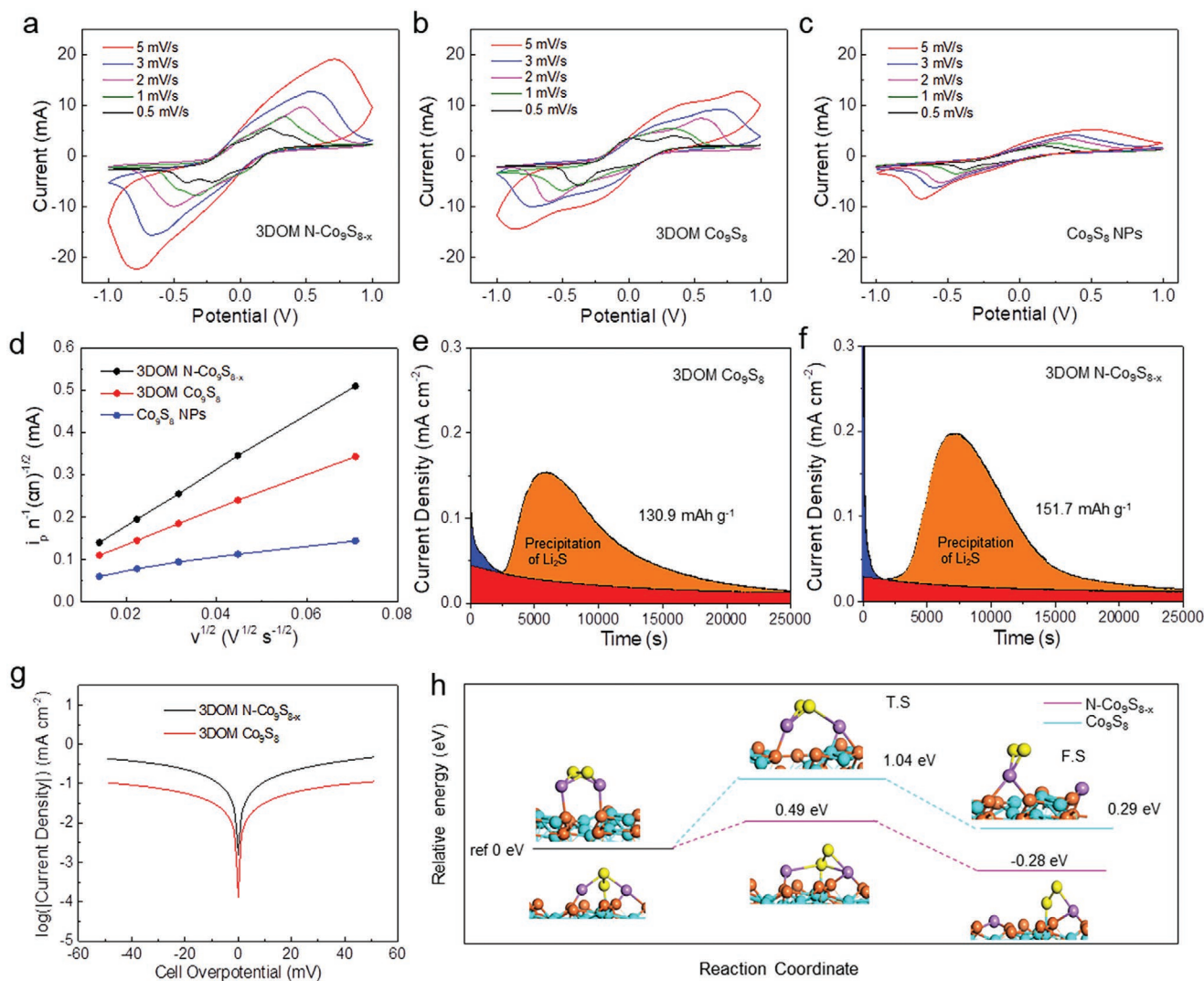


**Figure 5.** Kinetic and catalytic performance of  $\text{Co}_9\text{S}_8$  NPs, 3DOM  $\text{Co}_9\text{S}_8$ , and 3DOM  $\text{N-Co}_9\text{S}_{8-x}$  host materials. Symmetrical CV curves of a) 3DOM  $\text{N-Co}_9\text{S}_{8-x}$ , b) 3DOM  $\text{Co}_9\text{S}_8$ , c)  $\text{Co}_9\text{S}_8$  NPs; d) Plot of anodic peak current ( $\text{Li}_2\text{S} \leftrightarrow \text{Li}_2\text{S}_x$ ) as a function of the square root of the scan rates; e, f) Potentiostatic discharge profiles of a  $\text{Li}_2\text{S}_8$ /tetraglyme solution on various surfaces at 2.05 V; g) Tafel plots of the  $\text{Li}_2\text{S}_6$  solution redox; h) energy profiles of  $\text{Li}_2\text{S}_2$  decomposition on  $\text{Co}_9\text{S}_8$  and  $\text{N-Co}_9\text{S}_{8-x}$  (T.S: transition state, F.S: final state).

In view of Li-S chemistry, 3DOM  $\text{N-Co}_9\text{S}_{8-x}/\text{S}$  composites were prepared by melt-impregnation method and employed as cathode material. The TGA analysis reveals its element sulfur loading of 69.4 wt%, as shown in Figure S10 in the Supporting Information. Besides, the STEM image and EDX elemental mapping suggests its uniform sulfur distribution on the surface (Figure S11, Supporting Information). The electrochemical performance of 3DOM  $\text{N-Co}_9\text{S}_{8-x}/\text{S}$  cathode was also evaluated. Figure 6a shows the galvanostatic discharge-charge profiles of different cathodes. The discharge plateaus around 2.35 and 2.1 V can be attributed to the reduction of sulfur to long-chain  $\text{LiPS}$  and further reduction to  $\text{Li}_2\text{S}_2$  and  $\text{Li}_2\text{S}$ . Obviously, 3DOM  $\text{N-Co}_9\text{S}_{8-x}$  shows the smallest potential hysteresis and highest discharge capacity of  $1301.5 \text{ mAh g}^{-1}$ , indicating its high sulfur utilization and improved reaction kinetics. The CV curves in Figure 6b also exhibit two reduction peaks, which is consistent with the discharge-charge profiles. The 3DOM  $\text{N-Co}_9\text{S}_{8-x}/\text{S}$

demonstrates the distinctive redox peaks with minimum potential difference, indicating its lowest polarization. Additionally, Figure 6c and Figure S12 (Supporting Information) present the best rate performance of 3DOM  $\text{N-Co}_9\text{S}_{8-x}$  by showing the highest discharge capacity of  $812.8 \text{ mAh g}^{-1}$  at 5 C and  $1193.9 \text{ mAh g}^{-1}$  after the current switched back to 0.2 C, indicating its highly reversible electrochemistry. The EIS spectrum of 3DOM  $\text{N-Co}_9\text{S}_{8-x}$  exhibits the smallest resistance for interfacial charge transfer process (Figure 6d). Both the rate performance and EIS results unveil the good kinetic behavior of 3DOM  $\text{N-Co}_9\text{S}_{8-x}$  attributed to its improved ion/electron transportation and superior  $\text{LiPS}$  catalytic effect. The cycling performance in Figure 6e demonstrates the highest discharge capacity of  $1056.2 \text{ mAh g}^{-1}$  with decent capacity retention of 84.8% over 100 cycles under the current density of 0.2 C, indicating its superior physical and chemical  $\text{LiPS}$  confinement. Attributed to these synergistic features, the 3DOM  $\text{N-Co}_9\text{S}_{8-x}/\text{S}$  electrode

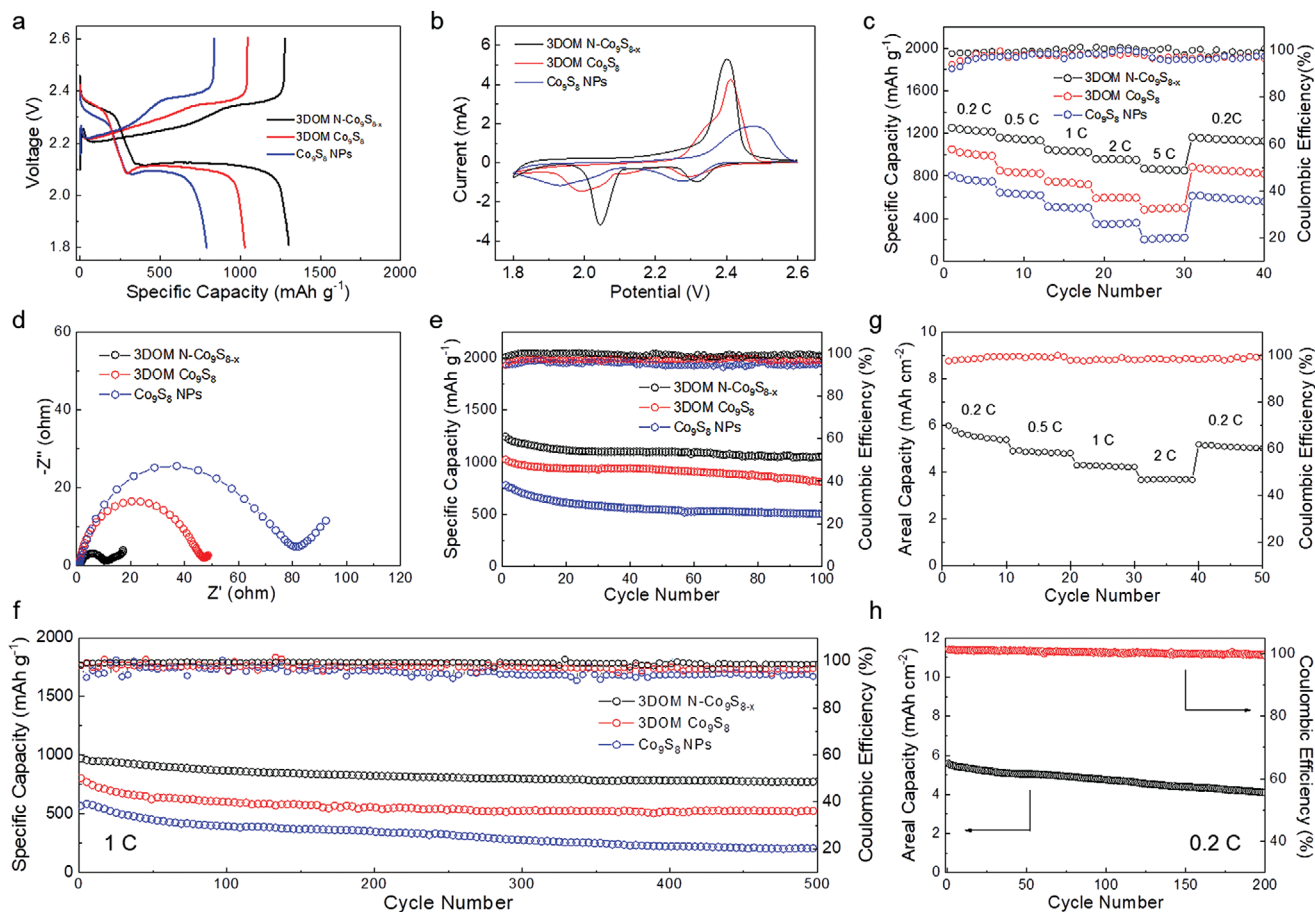


**Figure 6.** Electrochemical performance of  $\text{Co}_9\text{S}_8$  NPs/S, 3DOM  $\text{Co}_9\text{S}_8$ /S, and 3DOM N- $\text{Co}_9\text{S}_{8-x}$ /S cathodes: a) Galvanostatic discharge–charge profiles under the current density of 0.2 C; b) CV curves with a scan rate of  $0.2 \text{ mV s}^{-1}$ ; c) rate performance; d) EIS spectra; e) cycling performance under the current density of 0.2 C; f) long-term cycling operation of those composites under the current density of 1 C. Electrochemical performance of 3DOM N- $\text{Co}_9\text{S}_{8-x}$  sulfur composites under raised sulfur loading of  $6.5 \text{ mg cm}^{-2}$ : g) rate performance and h) cycling performance under the current density of 0.2 C.

achieves a high discharge capacity of  $927.8 \text{ mAh g}^{-1}$  after 500 cycles at 1 C (Figure 6f), corresponding to a remarkable cyclic stability with a low capacity fading rate of 0.04% per cycle. Even under raised current density of 2 C, 3DOM N- $\text{Co}_9\text{S}_{8-x}$ /S cathode still delivers a high discharge capacity of  $692 \text{ mAh g}^{-1}$  over 500 cycles with a low capacity fading rate of 0.12% per cycle and high average Coulombic efficiency, indicating its admirable cyclic stability attributed to its structural superiorities (Figure S13, Supporting Information). Note that, to evaluate the nitrogen doping effect of sulfur immobilization in 3DOM N- $\text{Co}_9\text{S}_{8-x}$ , we have also synthesized the 3DOM N- $\text{Co}_9\text{S}_8$  that treated under a short duration under  $\text{NH}_3$  atmosphere (5 min). The XRD pattern reveals that 3DOM N- $\text{Co}_9\text{S}_8$  shows similar structure feature comparing with 3DOM N- $\text{Co}_9\text{S}_{8-x}$  while no sulfur vacancies can be observed in 3DOM N- $\text{Co}_9\text{S}_8$  (Figure S14A,B, Supporting Information). Also, 3DOM N- $\text{Co}_9\text{S}_8$ /S cathode demonstrates a higher discharge capacity of  $1098.6 \text{ mAh g}^{-1}$  than that of 3DOM  $\text{Co}_9\text{S}_8$ /S ( $1025 \text{ mAh g}^{-1}$ ). However, this capacity is still lower than that of 3DOM N- $\text{Co}_9\text{S}_{8-x}$ /S ( $1244.9 \text{ mAh g}^{-1}$ ), indicating the insufficient LiPS adsorption and catalytic effect of 3DOM N- $\text{Co}_9\text{S}_8$ . Meanwhile, the cycling performance of 3DOM N- $\text{Co}_9\text{S}_8$ /S cathode exhibits a high discharge capacity of

$861.9 \text{ mAh g}^{-1}$  after 100 cycles with a decent capacity retention of 80.5%. This capacity retention of 3DOM  $\text{Co}_9\text{S}_8$ /S (79.1%) is still lower than that of 3DOM N- $\text{Co}_9\text{S}_{8-x}$ /S. This result indicates that the nitrogen doping effect of 3DOM N- $\text{Co}_9\text{S}_8$  framework slightly enhances the LiPS adsorption and electronic conduction, which improved the Li–S performance to some extent. Benefited from defect implantation, the 3DOM N- $\text{Co}_9\text{S}_{8-x}$  significantly improves the electronic conduction, LiPS adsorption and catalytic conversion, rendering the best electrochemical performance. This result highlighted the significance of defect engineering in our material design strategy (Figure S14C,D, Supporting Information).

To realize higher energy density requirement for Li–S batteries practicalization, the sulfur electrode should achieve decent electrochemical performance under raised sulfur loading and low E/S ratio. Figure S15 in the Supporting Information shows the galvanostatic discharge–charge curves of 3DOM N- $\text{Co}_9\text{S}_{8-x}$  sulfur composites electrode at different current densities under high sulfur loading of  $6.5 \text{ mg cm}^{-2}$  and low electrolyte sulfur (E/S) ratio of 5. Clearly, the profile still demonstrates two discharge plateaus even at 2 C, implying its good sulfur utilization and expedite reaction kinetics. Figure 6g manifests a high

initial capacity above 5.9 mAh cm<sup>-2</sup> of 3DOM N-Co<sub>9</sub>S<sub>8-x</sub> sulfur composite and its good rate capability up to 2 C. Furthermore, the stable long-term operation also clarifies its good cyclic stability and high areal capacity above 4 mAh cm<sup>-2</sup> after 200 cycles (Figure 6h). The good Li-S performance is attributed to the synergistically combination of architectural and structural superiorities of 3DOM N-Co<sub>9</sub>S<sub>8-x</sub>. The highly porous 3DOM N-Co<sub>9</sub>S<sub>8-x</sub> homogenizes sulfur distribution, retains electrolyte and alleviates volume expansion within the electrode. Meanwhile, the strong sulfur immobilizations and catalytic effect further ensures high sulfur utilization, efficient LiPS shuttling inhabitation and redox kinetics acceleration, leading to significantly prolonged life span of the Li-S batteries.

### 3. Conclusion

In the present study, we have employed surface engineering strategy to design 3DOM N-Co<sub>9</sub>S<sub>8-x</sub> material as multifunctional sulfur immobilizer toward enhanced Li-S electrochemistry. The 3DOM structure homogenizes sulfur distribution, provides vast active interfaces and reduced ion diffusion pathway to expedite redox reaction. The hierarchical porosity of 3DOM N-Co<sub>9</sub>S<sub>8-x</sub> affords large void interior to store electrolyte and accommodate volume expansion. Meanwhile, the defect engineering further introduces N substitution into Co<sub>9</sub>S<sub>8</sub> to induce the transformation of some CoS<sub>4</sub> tetrahedron to CoS<sub>6</sub> octahedra, leaving abundant S vacancies on its octahedral sites. The gradually increased S vacancies during electrochemical process further magnifies the adsorption capability and conversion kinetics of LiPS. Attributed to these superiorities, the 3DOM N-Co<sub>9</sub>S<sub>8-x</sub>/S cathode exhibits high sulfur utilization, enhanced LiPS chemisorption and electrocatalytic activity, leading to superior battery cyclability with a low capacity fading rate of 0.04% per cycle over 500 cycles at 1 C, good rate capability up to 5 C, and high areal capacity of 5.9 mAh cm<sup>-2</sup>. This design strategy offers a synergistic combination of architecture and defects engineering to enhance LiPS confinement and catalytic conversion, thereby enabling Li-S batteries with excellent sulfur kinetics and promoting its practical application.

### 4. Experimental Section

**Material Synthesis:** The 3DOM Co<sub>9</sub>S<sub>8</sub> composites were prepared using PS spheres as template. The PS spheres had an average diameter of ≈200 nm and were synthesized through emulsion polymerization using styrene, polyvinylpyrrolidone (PVP), potassium persulfate, and DDI water. Details on the preparation of PS spheres can be found in the literature. For the development of 3DOM N-Co<sub>9</sub>S<sub>8-x</sub>, 1.50 g cobalt sulfate [Co(SO<sub>4</sub>)<sub>2</sub> · 4 H<sub>2</sub>O] and 0.5 g thiourea (CH<sub>4</sub>N<sub>2</sub>S) were dissolved in a 10.5 mL solution that consist of methanol (MeOH) and hydrochloric acid (HCl) [MeOH: HCl volumetric ratio = 20:1]. The as-obtained precursor solution was added drop-wisely to the PS template (1 mL precursor: 0.2 g PS) under vacuum filtration. The infiltrated PS template was dried overnight at room temperature and transferred to furnace and calcination under NH<sub>3</sub> atmosphere at 500 °C for 20 min.

### Supporting Information

Supporting Information is available from the Wiley Online Library or from the author.

### Acknowledgements

G.L. and D.L. contributed equally to this work. The authors would like to acknowledge the financial support from University of Waterloo and the Natural Sciences and Engineering Research Council of Canada. The author would also like to acknowledge Qunfeng Xiao, Ya-Ping Deng, and Jianbin Zhu for their help with the XAS characterization in Canadian Light Source and Andrei Carmen for TEM characterization in Canadian Center of Electron Microscopy in McMaster University.

### Conflict of Interest

The authors declare no conflict of interest.

### Keywords

cobalt sulfide, defect engineering, lithium-sulfur batteries, macroporous-mesoporous, S vacancy

Received: February 20, 2020

Revised: June 1, 2020

Published online: August 9, 2020

- [1] a) G. Li, D. Luo, X. Wang, M. H. Seo, S. Hemmati, A. Yu, Z. Chen, *Adv. Funct. Mater.* **2017**, *27*, 1702562; b) G. Li, W. Lei, D. Luo, Y.-P. Deng, D. Wang, Z. Chen, *Adv. Energy Mater.* **2017**, *8*, 1702381; c) Y. Yang, H. Xu, S. Wang, Y. Deng, X. Qin, X. Qin, G. Chen, *Electrochim. Acta* **2019**, *297*, 641.
- [2] a) B. Y. Guan, A. Kushima, L. Yu, S. Li, J. Li, X. W. D. Lou, *Adv. Mater.* **2017**, *29*, 1605902; b) G. Li, S. Wang, Y. Zhang, M. Li, Z. Chen, J. Lu, *Adv. Mater.* **2018**, *30*, 1705590; c) D. Luo, G. Li, Y.-P. Deng, Z. Zhang, J. Li, R. Liang, M. Li, Y. Jiang, W. Zhang, Y. Liu, W. Lei, A. Yu, Z. Chen, *Adv. Energy Mater.* **2019**, *9*, 1900228.
- [3] a) H. Yuan, H.-J. Peng, B.-Q. Li, J. Xie, L. Kong, M. Zhao, X. Chen, J.-Q. Huang, Q. Zhang, *Adv. Energy Mater.* **2019**, *9*, 1802768; b) Z. Wang, J. Shen, J. Liu, X. Xu, Z. Liu, R. Hu, L. Yang, Y. Feng, J. Liu, Z. Shi, L. Ouyang, Y. Yu, M. Zhu, *Adv. Mater.* **2019**, *31*, 1902228.
- [4] a) H. J. Peng, Z. W. Zhang, J. Q. Huang, G. Zhang, J. Xie, W. T. Xu, J. L. Shi, X. Chen, X. B. Cheng, Q. Zhang, *Adv. Mater.* **2016**, *28*, 9551; b) X. Li, X. Li, M. N. Banis, B. Wang, A. Lushington, X. Cui, R. Li, T.-K. Sham, X. Sun, *J. Mater. Chem. A* **2014**, *2*, 12866.
- [5] Y. Zhang, L. Sun, H. Li, T. Tan, J. Li, *J. Alloys Compd.* **2018**, *739*, 290.
- [6] a) H.-J. Peng, J.-Q. Huang, X.-B. Cheng, Q. Zhang, *Adv. Energy Mater.* **2017**, *7*, 1700260; b) Z. Li, C. Li, X. Ge, J. Ma, Z. Zhang, Q. Li, C. Wang, L. Yin, *Nano Energy* **2016**, *23*, 15.
- [7] B. Y. Hao, H. Li, W. Lv, Y. B. Zhang, S. Z. Niu, Q. Qi, S. J. Xiao, J. Li, F. Y. Kang, Q. H. Yang, *Nano Energy* **2019**, *60*, 305.
- [8] M. Li, Y. Zhang, Z. Bai, W. W. Liu, T. Liu, J. Gim, G. Jiang, Y. Yuan, D. Luo, K. Feng, R. S. Yassar, X. Wang, Z. Chen, J. Lu, *Adv. Mater.* **2018**, *30*, 1804271.
- [9] W. Xue, Z. Shi, L. Suo, C. Wang, Z. Wang, H. Wang, K. P. So, A. Maurano, D. Yu, Y. Chen, L. Qie, Z. Zhu, G. Xu, J. Kong, J. Li, *Nat. Energy* **2019**, *4*, 374.
- [10] a) Z. Y. Wang, L. Wang, S. Liu, G. R. Li, X. P. Gao, *Adv. Funct. Mater.* **2019**, *29*, 1901051; b) D. Luo, Z. Zhang, G. Li, S. Cheng, S. Li, J. Li, R. Gao, M. Li, S. Sy, Y. P. Deng, Y. Jiang, Y. Zhu, H. Dou, Y. Hu, A. Yu, Z. Chen, *ACS Nano* **2020**, *14*, 4849.
- [11] K. Xi, D. He, C. Harris, Y. Wang, C. Lai, H. Li, P. R. Coxon, S. Ding, C. Wang, R. V. Kumar, *Adv. Sci.* **2019**, *6*, 1800815.

- [12] Q. Pang, D. Kundu, L. F. Nazar, *Mater. Horiz.* **2016**, *3*, 130.
- [13] G. Lui, G. Li, X. Wang, G. Jiang, E. Lin, M. Fowler, A. Yu, Z. Chen, *Nano Energy* **2016**, *24*, 72.
- [14] D. Luo, Y. P. Deng, X. Wang, G. Li, J. Wu, J. Fu, W. Lei, R. Liang, Y. Liu, Y. Ding, A. Yu, Z. Chen, *ACS Nano* **2017**, *11*, 11521.
- [15] Z. Zhang, Y. P. Deng, Z. Xing, D. Luo, S. Sy, Z. P. Cano, G. Liu, Y. Jiang, Z. Chen, *ACS Nano* **2019**, *13*, 7062.
- [16] L.-L. Feng, M. Fan, Y. Wu, Y. Liu, G.-D. Li, H. Chen, W. Chen, D. Wang, X. Zou, *J. Mater. Chem. A* **2016**, *4*, 6860.
- [17] B. Q. Li, C. X. Zhao, S. Chen, J. N. Liu, X. Chen, L. Song, Q. Zhang, *Adv. Mater.* **2019**, *31*, 1900592.
- [18] J. Li, W. Li, Y. You, A. Manthiram, *Adv. Energy Mater.* **2018**, *8*, 1801957.
- [19] Z. L. Wang, J. S. Yin, Y. D. Jiang, *Micron* **2000**, *31*, 571.
- [20] J. E. Kleibecker, E.-M. Choi, E. D. Jones, T.-M. Yu, B. Sala, B. A. MacLaren, D. Kepaptsoglou, D. Hernandez-Maldonado, Q. M. Ramasse, L. Jones, J. Barthel, I. MacLaren, J. L. MacManus-Driscoll, *NPG Asia Mater.* **2017**, *9*, 406.
- [21] Y. Zhang, Z. Mu, C. Yang, Z. Xu, S. Zhang, X. Zhang, Y. Li, J. Lai, Z. Sun, Y. Yang, Y. Chao, C. Li, X. Ge, W. Yang, S. Guo, *Adv. Funct. Mater.* **2018**, *28*, 1707578.
- [22] W. Cai, G. Li, D. Luo, G. Xiao, S. Zhu, Y. Zhao, Z. Chen, Y. Zhu, Y. Qian, *Adv. Energy Mater.* **2018**, *8*, 1802561.
- [23] O. Bunau, Y. Joly, *J. Phys. Condens. Matter* **2009**, *21*, 345501.
- [24] S. M. A. M. Bouwens, J. A. R. Van Veen, D. C. Koningsberger, V. H. J. De Beer, R. Prins, *J. Phys. Chem.* **1991**, *95*, 123.
- [25] Q. Pang, C. Y. Kwok, D. Kundu, X. Liang, L. F. Nazar, *Joule* **2019**, *3*, 136.
- [26] Z. Du, X. Chen, W. Hu, C. Chuang, S. Xie, A. Hu, W. Yan, X. Kong, X. Wu, H. Ji, L. J. Wan, *J. Am. Chem. Soc.* **2019**, *141*, 3977.